

Nano-scale mechanics of colloidal C–S–H gels

Cite this: *Soft Matter*, 2014, 10, 491Enrico Masoero,^{*ab} Emanuela Del Gado,^c Roland J.-M. Pellenq,^{bd} Sidney Yip^e and Franz-Josef Ulm^b

Received 2nd July 2013

Accepted 28th October 2013

DOI: 10.1039/c3sm51815a

www.rsc.org/softmatter

Gels of calcium–silicate–hydrates (C–S–H) are the glue that is largely responsible for the mechanical properties of cement. Despite their practical relevance, their nano-scale structure and mechanics are still mainly unexplored, because of the difficulties in characterizing them in a complex material like cement. We propose a colloidal model to investigate the gel mechanics emerging in the critical range of length-scales from several tens to hundreds of nanometers. We show that the size polydispersity of the hydrates and size-dependent effective interactions can explain the mechanical heterogeneities detected in nano-indentation experiments. We also show how these features control the arising of irreversible structural rearrangements under deformation, which are good candidates as nano-scale mechanisms underlying mechanical aging and slow structural relaxation in the gels.

1 Introduction

Calcium–silicate–hydrates (C–S–H) form inorganic hydrogels with a variety of complex nano-scale structures,^{1–4} depending on the external chemical and physical environments. These gels are the main binder phase of ordinary cements, determining to a large extent the properties of the most widely used material on Earth. The C–S–H phase in cement forms upon chemical reaction between the fine clinker powder (containing calcium–silicates) and water, and precipitates from the supersaturated pore solution rich in calcium and silicon ions. Controlling the complex chemo–mechanical processes that underlie the precipitation of the hydrates and the development of the cohesive gel is a strenuous undertaking. In the experimental systems it has been so far impossible to separate the different basic mechanisms from their combined effects. In particular this would require a deep understanding, far from being reached, of transport and aggregation phenomena that are also typical of other colloidal and soft-matter systems. In the case of cements, such phenomena take place under far-from-equilibrium conditions that are closely intertwined with the chemical evolution of the environment. Although several aspects of this chemical evolution, from the dissolution of the clinker to the precipitation of C–S–H, have been systematically investigated,^{5–7} the development of

the physical properties of the gel is still mainly unexplored. Hence, for example, it is still fundamentally not known which features of the nano-scale structure of the gel are important for the overall mechanics of the material. Experiments have recently shown that the C–S–H dense gels in hardened cement paste, *i.e.* at the end of hydration, still display an inexorably slow mechanical aging and indicated that this affects the material performance up to the level of concrete structures.^{8,9} Specific structural features of the C–S–H gels, developed under the non-equilibrium conditions of hydration, might control mechanical aging and, once identified, could be used as levers to control also other aspects of the non-linear mechanical response of the material. Achieving such understanding could lead to a real breakthrough on how to design new *green* formulations of cement without sacrificing the mechanical performance.

In C–S–H gels the range of length-scales from several tens to hundreds of nanometers, typical of soft matter systems, is particularly crucial. The structural heterogeneity and lack of long-range order that clearly arise over these length-scales ultimately determine the mechanical response.¹⁰ This range of length-scales has been hardly addressed by modeling and computational studies that, so far, have been mostly focused on sub-nanometer scales or to the other end on the micrometer-scale structure of the C–S–H phase.^{11–14} With the aim of investigating these intermediate length scales, we have recently proposed a new colloidal model for the C–S–H gels.¹⁵ We described the dense C–S–H gel as a polydisperse assembly of nano-scale colloidal (spherical) particles that interact *via* a simple attractive potential well. The attraction strength and width were set using information from experiments and atomistic simulations.¹¹ We employed a Monte Carlo procedure to generate disordered assemblies of such particles. The results of our numerical mechanical tests showed that the indentation moduli measured in experiment can be ascribed to large size

^aSchool of Civil Engineering and Geosciences, Newcastle University, Newcastle upon Tyne, NE1 7RU, UK. E-mail: enrico.masoero@newcastle.ac.uk; Tel: +44 (0)191 222 7687

^bDepartment of Civil and Environmental Engineering, Massachusetts Institute of Technology, 77 Massachusetts Avenue, Cambridge, MA 02139, USA

^cInstitute for Building Materials, ETH Zürich, 8093 Zurich, Switzerland

^dCINaM, CNRS and Aix-Marseille University, Campus de Luminy, 13288 Marseille Cedex 09, France

^eDepartment of Nuclear Science and Engineering, Massachusetts Institute of Technology, Cambridge 02139, USA

polydispersities of the hydrates in the gels,¹⁵ information that is not accessible experimentally. These first results open a whole set of new questions. In particular, TEM images and neutron scattering experiments^{6,16,17} indicate rather anisotropic shapes and contact areas with finite extent, which is likely to significantly change the mechanics of the assemblies. Although here we do not address the anisotropy of the particles directly, we consider the effect of finite contact areas by introducing size dependent interactions in our model. We then investigate the nano-scale mechanics of the structures obtained with different degrees of polydispersity. The results of our mechanical tests indicate excellent agreement with the elastic moduli of the C–S–H gel as measured by nanoindentation experiments. Starting from this, we analyze the role of polydispersity in the onset of plastic events and we show that structural heterogeneities of the type considered here can be crucial in C–S–H gels.

The paper is organized as follows: in Section 2 we describe the model and the numerical simulations. In Section 3 we perform numerical studies of the mechanical response of the model C–S–H gels under small and large deformations. In particular, after discussing the elastic behavior in Section 3.1, we analyze irreversible processes underlying the onset of non-linear response under shear in Section 3.2. In Section 3.3 we show that the irreversible processes are directly related to stress drops and local non-affine rearrangements, and that size polydispersity plays an important role. Conclusions and an outlook for this work are discussed in Section 4.

2 C–S–H gel structures: polydispersity, interactions, and generation algorithm

We consider that, by the end of the hydration process, a dense cohesive C–S–H gel is formed and that its sub-micrometer structure can be well represented by a disordered assembly of colloidal polydisperse hydrates. This accounts for attractive effective interactions that introduce spatial correlations as well as correlations between sizes and positions of the particles in the structure. Hence we produce disordered sub-micrometer structures using a Monte Carlo space filling algorithm that minimizes the interaction energy (see Fig. 1).¹⁵

For the effective interactions between the colloidal particles we use a simple well potential (see Fig. 2):

$$U_{ij}(r_{ij}) = 4\epsilon(\sigma_i, \sigma_j) \left[\left(\frac{\bar{\sigma}_{ij}}{r_{ij}} \right)^{2\alpha} - \left(\frac{\bar{\sigma}_{ij}}{r_{ij}} \right)^\alpha \right]. \quad (1)$$

where σ_i and σ_j are the diameters of particles i and j , r_{ij} is their relative distance, and $\epsilon(\sigma_i, \sigma_j)$ is the well depth between them. α controls how narrow the potential well is, and $\bar{\sigma}_{ij} = (\sigma_i + \sigma_j)/2$.

The internal, sub-nanometric structure of C–S–H hydrates is known to be anisotropic, as it is characterized by silicate chains and calcium oxide layers with water layers in the interlaminal spaces between them.^{18–20} In the crystalline form (tobermorite), the silicate chains are continuous. By contrast, the additional calcium that is usually present in the C–S–H in cement causes distortions of the layers and trimming of the silicate chains.¹¹

This complex molecular structure translates into effective interactions among hydrates in the C–S–H gels which have been the subject of an intense debate in the last few years, and are still under investigation.^{21,22} In the absence of deeper understanding, we assume that anisotropy is lost, on average, over distances of few nanometers, due to random orientation of the layers. We therefore consider only central forces, although more complicated effective interactions can be certainly implemented in our approach and will be the subject of future studies. We consider that the hydrates get strongly bonded in the gel through the calcium–silicate layers and therefore the interaction strength must depend, among other factors, on the contact area between pairs of particles, *viz.* the size of the interface between them. We account for this by considering a size dependent interaction strength $\epsilon(\sigma_i, \sigma_j)$. Considering the two hydrates in contact as two springs in series leads to $\epsilon(\sigma_i, \sigma_j) \approx A_0 \beta_{ij} \bar{\sigma}_{ij}^3$. A_0 is a prefactor proportional to the Young modulus Y of a hydrate† (assumed equal for the two particles). $\beta_{ij} = \sigma_i \sigma_j / \bar{\sigma}_{ij}^2$ is a correction term that arises from the serial arrangement, and was not included in the previous version of the interaction potential in ref. 15. It is interesting to note that a similar type of scaling $\epsilon(\sigma_i, \sigma_j) \propto \bar{\sigma}_{ij}^3$ would emerge from a Hertz type of contact²³ between particles i and j , with the difference that the Hertz contact model accounts only for repulsion while our formulation includes cohesion as well.

The energy scale for the cohesion between particles i and j , *i.e.* the prefactor A_0 in $\epsilon(\sigma_i, \sigma_j)$, and α in eqn (1) can be set on the basis of properties measured from atomistic simulations.^{12,24} From the shear strain at rupture $\gamma_u \approx 10\%$ measured for a stack of silicate layers we can estimate an equivalent uniaxial strain at tensile rupture $\epsilon_u = (\sqrt{\gamma_u^2 + 2} - 1)/\sqrt{2} \approx 5\%$ (*viz.* the tensile principal strain associated with a pure shear strain γ_u). The attractive force from eqn (1) is null at a distance $r_m = \sqrt[3]{2} \bar{\sigma}_{ij}$: from this, for simplicity we can redefine the diameter of particle i as $\sigma_{0,i} = \sqrt[3]{2} \sigma_i$. The maximum tensile force is attained

at a distance $r_u = \sqrt[3]{\frac{4\alpha + 2}{\alpha + 1}} \bar{\sigma}_{ij}$, corresponding to a strain $\epsilon_u = (r_u - r_m)/r_m$, and, by choosing $\alpha = 14$, this gives $\epsilon_u = 4.82\%$, in reasonably good agreement with the indications from atomistic simulations. A relatively narrow potential well, as given by $\alpha = 14$, is also consistent with AFM measurements.²² If we assume that the cohesive strength between our colloidal particles is basically the same as the cohesion between calcium–silicate layers within each hydrate, we can set the energy scale† using the value of the Young modulus $Y = 63.6$ GPa obtained from atomistic simulations performed on calcium–silicate–hydrates of a few nanometers.²⁴ This corresponds to interaction strengths ranging between $1000 k_B T$ and $1.5 \times 10^6 k_B T$ ($T = 300$ K), respectively for the smallest ($\sigma = 3$ nm) and the largest ($\sigma = 35$ nm) particle sizes that we consider here.

We start from an initially empty cubic simulation box of linear size L in contact with an infinite reservoir of C–S–H

† A serial arrangement of two springs in series, with $Y\pi\left(\frac{\sigma_{0,i}}{2}\right)^2/\frac{\sigma_{0,i}}{2}$ being the stiffness of the spring associated with the i^{th} particle, leads to $\epsilon(\sigma_i, \sigma_j) = 0.002324 Y \beta_{ij}(\sigma_i, \sigma_j) \bar{\sigma}_{ij}^3$.

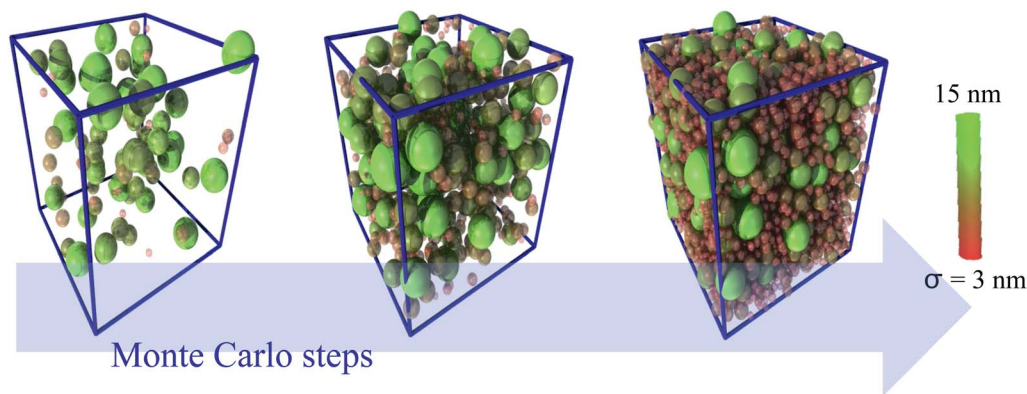


Fig. 1 Snapshots from a simulation to generate a model C–S–H structure extracting particles from a reservoir with polydispersity $\delta = 0.38$. The color code indicates the particle size that, in our model, is indicative also of the strength of cohesion. Due to space filling, as the simulation advances the small particles increase in number compared to the large ones.

nanoparticles. The linear size σ of the particles in the reservoir follows a uniform distribution between a minimum σ_m and a maximum σ_M value. The standard deviation δ of this distribution in units of $1/2(\sigma_M + \sigma_m)$ defines the polydispersity. A particle size is randomly extracted from the reservoir and an insertion at a random location in the simulation box is tried. The insertion is accepted with probability $P_{\text{creat}} = \exp(-\Delta U/k_B T)$, where k_B is the Boltzmann constant and ΔU is the difference in total interaction energy caused by the trial insertion. We also allow for particle displacements within the box, trying $D_p N$ Metropolis Monte Carlo moves in the NVT ensemble after every trial insertion. N is the number of particles in the box, which increases with the simulation time, and D_p is an arbitrary “delay” parameter, qualitatively inverse to a precipitation rate. The algorithm proceeds until N approaches a constant maximum value, *i.e.* space is filled. A typical sequence of snapshots is shown in Fig. 1. In all simulations discussed here, the delay parameter D_p is kept fixed to 10^{-2} . Four different polydispersities are considered (see Table 1) and we use between 10^7 and 2×10^9 Monte Carlo steps, depending on the simulation.

We compute an approximate solid volume fraction, or packing fraction $\phi = \sum_i \pi/6 \sigma_{0,i}^3 / L^3$, where we use the particle

diameter defined previously $\sigma_{0,i} = \sqrt[4]{2}\sigma_i$. Fig. 3 shows that, as expected, a better packing is achieved at high polydispersity.¹⁵ As space filling proceeds, inserting large particles becomes unlikely while smaller particles can still fit (see Fig. 1). This

causes the final particle size distribution to differ significantly from the uniform distribution in the reservoir. The final particle size distributions are geometric,^{15,25} as shown in Fig. 4.

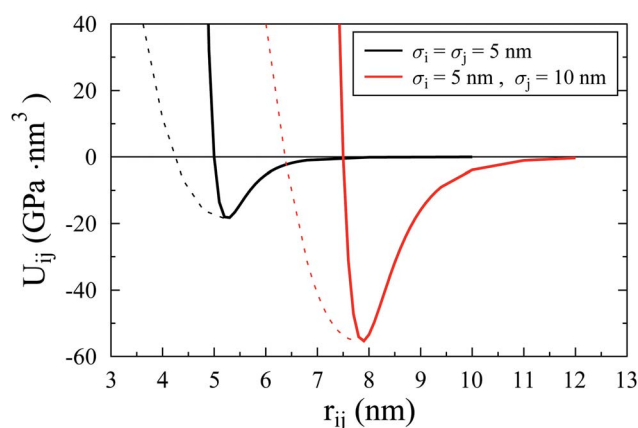


Fig. 2 Interaction potential for pairs of particles with sizes σ_i and σ_j . For comparison, the dashed lines show repulsive terms obtained from the Hertz contact model with a modulus $M = 65$ GPa.

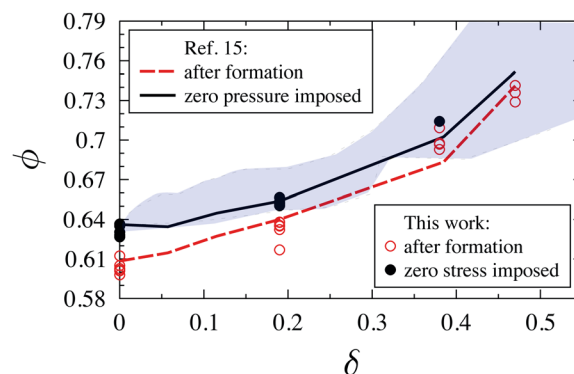


Fig. 3 Effect of polydispersity δ on the packing fraction ϕ . We show results for systems both just after their formation and after the subsequent relaxation to zero stress or pressure, which generally reduces the volume and therefore increases ϕ . The shaded region refers to jammed hard sphere packings.²⁶

Table 1 Explored polydispersities δ , corresponding minimum and maximum particle sizes (σ_m and σ_M), range of explored linear size L of the cubic simulation box, and range of the number of particles N obtained at the end of the space filling process

δ	σ_m (nm)	σ_M (nm)	L (nm)	N
0	5	5	40–60	504–6968
0.19	3.5	7	50–70	1495–4087
0.38	3	15	42–90	907–7112
0.47	3.5	35	92–190	3731–17 670

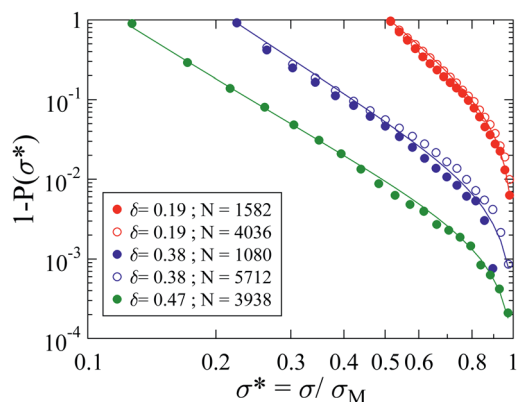


Fig. 4 Dimensionless particle size σ^* distributions. $P(\sigma^*)$ is the cumulative probability. The solid lines are fits assuming a geometric size distribution, with shape parameters^{15,25} -4.2 , -3.25 , and -2.9 respectively for the cases with $\delta = 0.19$, 0.38 , and 0.47 .

3 Mechanical properties of the polydisperse C–S–H structures

In this section we investigate the mechanical properties of the model C–S–H structures obtained from the simulations. The structures at the end of the space filling are all under negative pressure, *i.e.* tensile (virial) normal stresses,²⁷ due to attractive interactions and periodic boundary conditions. To mimic more realistic ambient conditions we relax the model structures to zero stress using the isotension isothermal NtT ensemble.^{28,29,†} Fig. 3 shows that the packing fraction increases for all δ values after relaxation and the results are consistent with those reported in ref. 15, as well as with the packing fractions of jammed, polydisperse hard spheres.²⁶ The new features of the potential implemented here do not seem to affect significantly the packing, whereas they do have an effect on the mechanical properties.

3.1 Elastic properties at zero stress

We characterize the elastic properties of the model C–S–H structures in terms of the tensor of elasticity. The tensor is computed keeping fixed the simulation box after equilibration to zero stress, and using the stress fluctuation method.³⁰ According to this method the tensor of elasticity $[C]$ (a 6×6 matrix in Voigt notation) is decomposed into a configurational contribution related to the second derivatives of the potential in eqn (1), and a stress fluctuation component that includes the temperature. For an isotropic material, the only non-zero values of C_{ij} are for $i, j \leq 3$ and for $i = j$. Table 2 shows a typical elastic tensor for one of our monodisperse configurations: there are some small deviations from the isotropic case, probably due to the finite size and to the fact that NtT relaxation leads to stresses that, although very small, are not exactly zero. Nevertheless, the

Table 2 Tensor of elastic constants (in GPa units) for the mono-disperse system with $N = 504$, in Voigt notation. The tensor is symmetric and the lower half is not shown for better readability. The terms for $i, j > 3$ and $i \neq j$ should be zero for isotropic materials

C_{ij}	$i = 1$	2	3	4	5	6
$j = 1$	30.92	17.61	20.99	−0.15	−0.18	0.58
2		31.21	18.82	1.25	−0.86	0.35
3			30.87	−1.34	0.93	0.41
4				6.87	−0.53	0.02
5					7.18	0.26
6						7.25

deviations from the isotropic case do not follow a clear trend and are small enough to assume that isotropy holds for the elastic properties of the systems. Polydispersity increases the finite terms of $[C]$, corresponding to higher stiffnesses, certainly due the higher packing fractions and different stress distribution attained. For an isotropic material, we can use the Voigt formulae to compute the bulk (K) and shear (G) moduli from the components of $[C]$ and obtain the indentation modulus M .^{8,31}

$$M = 4G \frac{3K + G}{3K + 4G}. \quad (2)$$

The indentation modulus is proportional to the stiffness of contact, *i.e.* the slope during unloading of the load-penetration curve obtained from indentation tests.⁸ Being the diameter of a nano-indenter's tip in the order of few hundreds of nanometers, the indentation modulus allows a direct comparison between our simulation results and nano-indentation experiments on C–S–H gels. In Fig. 5 we plot the indentation moduli computed for our model structures as a function of their packing fractions. Experimental data for a white cement paste¹¹ are also shown and indicate excellent agreement. The present study improves significantly the agreement with the experimental results compared to a previous study,¹⁵ where the contact area between particles was approximated as $\bar{\sigma}_{ij}^2$ in the effective interaction potential (*cf.* eqn (1)). This led to an overestimation of indentation moduli in ref. 15, although the linear trend with ϕ was preserved.

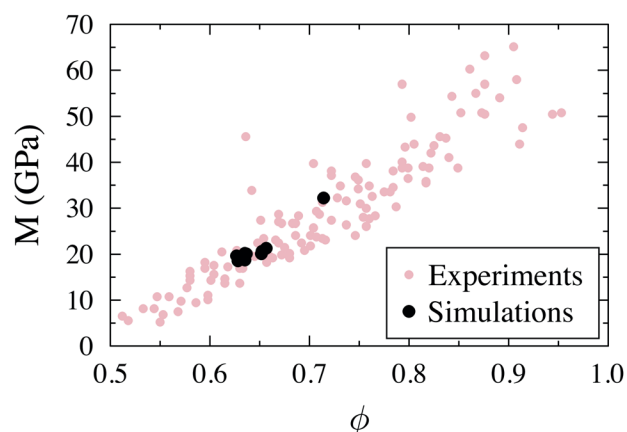


Fig. 5 Indentation moduli vs. packing fraction. Comparison between our simulations and nano-indentation experiments.¹¹

† We prefer the NtT over the isobaric NPT ensemble because relaxing all six stress components independently toward zero provides a reference configuration that is appropriate to any type of subsequent test conditions, *e.g.* volumetric, deviatoric or uniaxial.

3.2 Shear deformations and irreversible rearrangements

Large deformations cause a nontrivial evolution of internal stresses in the C-S-H gels. In order to investigate this, we subjected the structures obtained for different polydispersities to a series of pure shear strain increments $\Delta\epsilon_{xz} = \Delta\epsilon_{zx} = 0.005$. Each strain increment is followed by 5×10^7 – 3×10^8 Monte Carlo trial displacements performed in the NhT ensemble, *i.e.* keeping the simulation box fixed, after which we compute the shear stress τ_{xz} . In Fig. 6 we plot the shear stress τ (*i.e.*, τ_{xz} averaged over statistically independent samples) as a function of the cumulative strain $\gamma = 2\sum\Delta\epsilon_{xz}$, for systems with different polydispersities. The data show that small cumulative strains ($\gamma \leq 0.03$) are accompanied by a first rapid increase of stresses in the material. At larger γ all systems undergo yielding at a stress level that increases significantly upon increasing the polydispersity. The yielding stress is a measure of strength, and nanoindentation experiments⁸ confirm that the strength of the C-S-H (quantified by the hardness) increases with its packing density, *i.e.* with the polydispersity in our model (see Fig. 3). The inset of Fig. 6 shows the shear moduli G evaluated at different γ values from the elastic tensor (see Section 3.1). The values at $\gamma = 0$ are obtained from the same elastic tensors as the indentation moduli in Fig. 5. As γ increases, the average values of the shear moduli change from the original one at $\gamma = 0$, suggesting that significant structural changes are taking place. This effect is particularly evident in the highly polydisperse systems ($\delta = 0.38$), but a more quantitative analysis would require a dedicated study.[§]

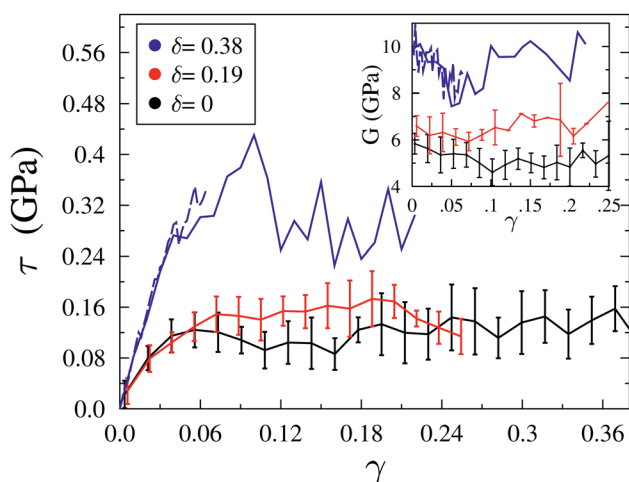


Fig. 6 Pure shear stress τ –strain γ tests for systems with different polydispersities δ (and packing fraction ϕ , which increases with δ , as shown in Fig. 3). The inset shows the evolution of the shear elastic modulus G during the tests. Averages and standard deviations have been computed from 13 statistically independent samples for $\delta = 0$ and 10 samples for $\delta = 0.19$. Two samples are shown for $\delta = 0.38$.

[§] It is worth reminding that the highly polydisperse systems may be more significantly affected by finite size effects.

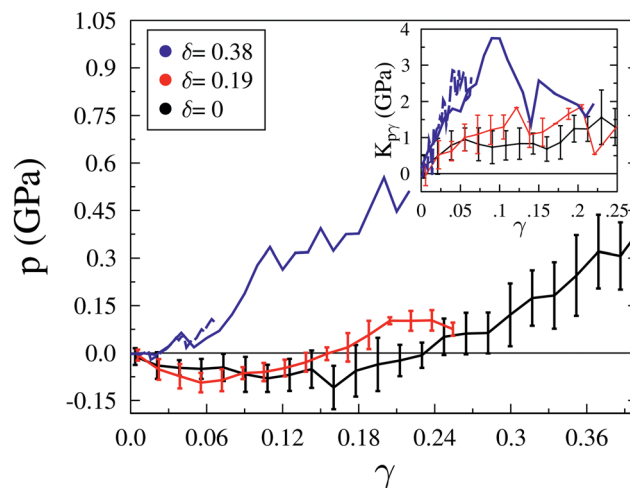


Fig. 7 Pressure p built up during the shear strain γ tests in Fig. 6, for systems with different polydispersities δ (and packing fraction ϕ , which increases with δ , as shown in Fig. 3). The inset shows the evolution of the anisotropy modulus $K_{p\gamma}$ during the tests.

The response to the cumulative shear strain is accompanied by a change in the pressure, as shown in Fig. 7. This indicates a coupling between the deviatoric and the hydrostatic components of the stress. In particular, the monodisperse and weakly polydisperse systems display a negative pressure when the strain γ is low, *i.e.*, they would contract under shear if the volume were allowed to relax under isobaric conditions at $p = 0$. By contrast, higher levels of stress in the monodisperse and weakly polydisperse systems induce an increasingly positive pressure: a tendency to dilate that is strongly reminiscent of dilation typical of granular, athermal systems.³² Interestingly, the highly polydisperse systems ($\delta = 0.38$, corresponding to the highest volume fraction) display positive pressure, *i.e.* a tendency to dilate, at all levels of applied strain. The correlations between τ and p correspond to an increase of the non-zero terms C_{15} , C_{25} , and C_{35} in the elastic tensor (*e.g.* in Table 2) and could therefore suggest stress-induced anisotropy.³³ We have quantified this buildup of anisotropy by computing a modulus $K_{p\gamma} = -(C_{15} + C_{25} + C_{35})/6$, obtained from $p = -1/3(C_{15} + C_{25} + C_{35})\epsilon_{xz}$. $K_{p\gamma}$ is plotted against γ in the inset of Fig. 7 and grows indeed with γ (for $\gamma \leq 0.1$) and with increasing polydispersity.

In order to distinguish between the reversible and the irreversible parts of the deformation, each configuration corresponding to (γ, τ) pairs in Fig. 6 is then relaxed back to $\tau = 0$. This is accomplished by varying the strain components $\epsilon_{xz} = \epsilon_{zx}$ of the simulation box in mixed NhT–NtT ensemble. In general the residual shear strain γ_{res} , after τ is relaxed back to zero, is not null, as it should instead be in the case of a fully elastic response. Fig. 8 shows that γ_{res} is continuously growing as a function of the shear strain γ applied before relaxation. The increase of γ_{res} with γ becomes more pronounced and approximately linear for strains $\gamma > 0.02$, for the systems with lower polydispersity, $\delta = 0$ and $\delta = 0.19$. For the more polydisperse systems, with $\delta = 0.38$, this occurs at a larger strain $\gamma > 0.05$.

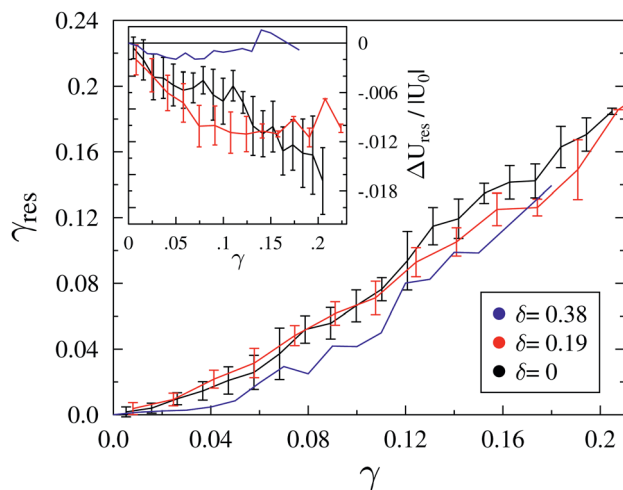


Fig. 8 Irreversible deformations: residual shear strain after relaxation back to zero shear stress $\tau = 0$ of systems previously loaded to γ (see Fig. 6). The systems have different polydispersities δ (and packing fraction ϕ , which increases with δ , as shown in Fig. 3). The inset shows the change of interaction energy after relaxation ΔU_{res} induced by the deformation γ , and divided by the absolute value original of interaction energy of the systems at zero strain and stress ($\gamma = 0$, $\tau = 0$). Averages and standard deviations were computed from 13 statistically equivalent samples for $\delta = 0$ and 6 samples for $\delta = 0.19$. One dataset for $\delta = 0.38$ is also shown.

These results indicate overall that the dense gels display a non-linear response characterized by yielding, mechanical instability, and structure recoveries, all accompanied by the development of anisotropy and probably associated with irreversible dynamical processes. This is also supported by the data in the inset of Fig. 8, which shows the internal energy U_{res} of the systems relaxed from γ back to $\tau = 0$. U_0 is the total internal energy of the original C-S-H structures at zero stress before the shear test, and $\Delta U_{\text{res}} = U_{\text{res}} - U_0$. The data indicate that the applied strain allows attaining better stability upon relaxing the stresses, with a residual internal energy that is always lower than the one of the initial configurations. For the monodisperse and weakly polydisperse systems this is consistent with the development of pressure in Fig. 7 and indicates a progressive compaction of the structures. Nevertheless, it is interesting to notice that also the highly polydisperse systems become more stable under shear, in spite of their tendency to dilate indicated by the positive pressure in Fig. 7. Finally, Fig. 7 indicates that despite the accumulated γ_{res} is comparable for all systems irrespective of their polydispersity δ , the change in potential energy is much more significant in the monodisperse and weakly polydisperse systems, which is probably due to their lower packing fraction ϕ (see Fig. 3).

3.3 Stress drops and local analysis of the non-affine displacements

To further investigate the irreversible dynamical processes that may underlie the mechanical instability associated with the yielding, we have analyzed the load curve of each sample separately. Fig. 9 shows a portion of the stress-strain curve of a

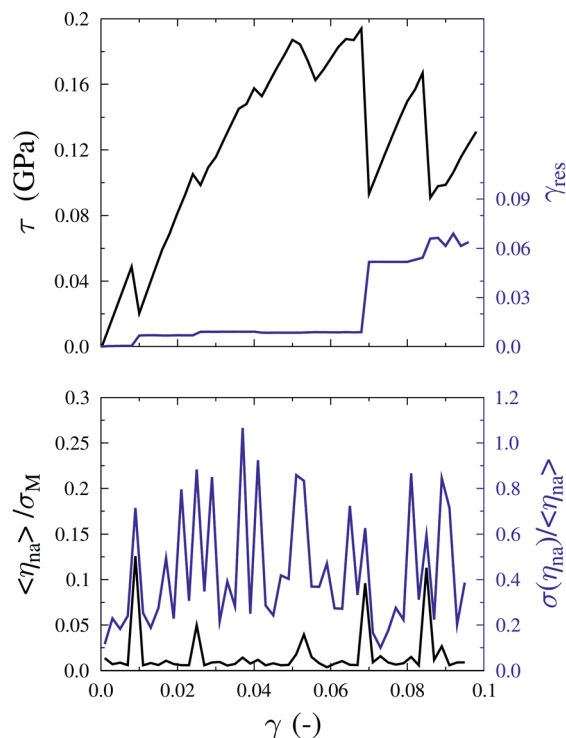


Fig. 9 Top: shear stress-strain curve and the corresponding accumulation of irreversible strain γ_{res} after relaxation back to $\tau = 0$, for the monodisperse systems with $N = 508$. Bottom: magnitude of the non-affine displacement vector averaged over the particles $\langle \eta_{\text{na}} \rangle$ and the corresponding standard deviation $\sigma(\eta_{\text{na}})$, associated with each strain increment.

monodisperse system with $N = 508$ and the accumulation of irreversible deformations γ_{res} .[¶] The curve displays sudden stress drops that are more dramatic compared to those in Fig. 6, where averages were taken over different samples. One can immediately recognize that these drops are directly correlated with a step increase of residual strains γ_{res} (upon relaxing the deformed structure back to $\tau = 0$), although not all stress drops are accompanied by irreversibility (quantified by γ_{res}). Before the first stress drop occurs ($\gamma < 0.01$ for the sample in Fig. 9) the system response is linear elastic, as indicated by its ability to completely relax the internal stresses developed under deformation without residual strains. We also observed sudden drops of pressure towards negative values in correspondence to the drops of shear stress. We have tested the possibility that, for the monodisperse systems, the drops of stress accompanied by a negative pressure and an overall decrease of interaction energy at rest (see the inset of Fig. 8) may be due to local crystallization. This seems not to be the case here, because we observe that in most of the cases the fraction of particles with local crystalline order decreases during the shear test. This

[¶] For illustrative purposes in Fig. 6, among all the systems that we analyzed, we decided to refer to a monodisperse one with very small size. The reason is that the effect of local irreversible deformation events on systems-level quantities, e.g. the magnitude of stress drops and the increase of γ_{res} , is more pronounced in small, monodisperse systems.

absence of crystallization in the monodisperse systems is consistent with the comparable behaviors of the monodisperse $\delta = 0$ and the weakly polydisperse systems $\delta = 0.19$ shown in Fig. 6–8, which have similar packing fractions (see Fig. 3). Possible reasons for the lack of crystallization^{34–37} include the constant-volume shear protocol that we employed, as opposed to a constant pressure one, and the narrow interaction potential (see Section 2).

For each strain increment, Fig. 9 shows also the average magnitude of the non-affine displacement vectors, averaged over all the particles in the box $\langle \eta_{\text{na}} \rangle$, and the corresponding standard deviations $\sigma(\eta_{\text{na}})$. Non-affine displacements always accompany the deformations of disordered solids, also within the elastic regime, but during irreversible events they are normally larger.^{38–40} Fig. 9 shows in fact that the magnitude of the average non-affine displacement $\langle \eta_{\text{na}} \rangle$ is dominated by such irreversible particle rearrangements. Furthermore, it is interesting to notice that the stress drops not corresponding to an irreversible displacement are instead captured by the ratio between the standard deviation of η_{na} and its average. This suggests that such events are more “local”, *i.e.* they involve a smaller number of particles (the standard deviation is in fact more sensitive to the tail of the distribution of η_{na}). Local events that cause instability but are not accompanied by irreversibility might be a signature of local mechanisms of elastic Eulerian instability.⁴¹

In order to study the effect of the polydispersity on the non-affine displacements, in Fig. 10 we plot the accumulated $\langle \eta_{\text{na}} \rangle$ for systems with different polydispersities, as a function of the cumulated shear strain. Fig. 10 shows that the total non-affine displacements increase continuously after yielding, when irreversible dynamical processes govern the non-linear response. The systems with high polydispersity $\delta = 0.38$ seem to accumulate an amount of average non-affine displacement comparable to those of weakly polydisperse ($\delta = 0.19$) and monodisperse ($\delta = 0$) systems.

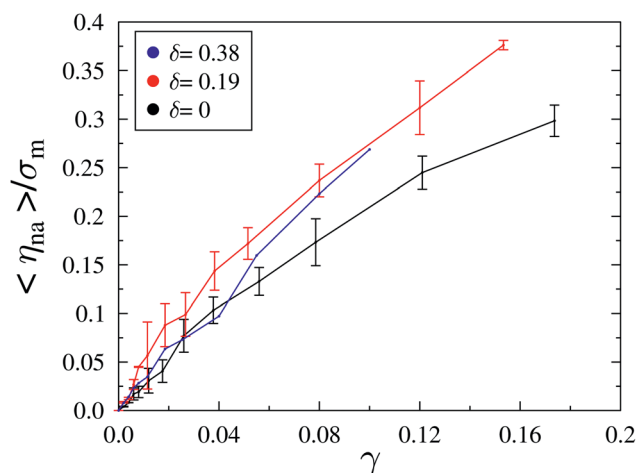


Fig. 10 Total non-affine displacements accumulated during the shear tests, between $\gamma = 0$ and γ . Averages and standard deviations were computed from four statistically equivalent samples for $\delta = 0$ and $\delta = 0.19$. One sample is shown for $\delta = 0.38$.

To further and more directly investigate the role of polydispersity, in Fig. 11 we plot the magnitude of non-affine displacements as a function of the particle diameters. Small particles experience larger non-affine displacements during an irreversible event, which indicates that they govern the accumulation of irreversibility. This concentration of non-affine displacements in the small particles is enhanced upon increasing the polydispersity, suggesting that large particles may behave as inclusions that hinder the development of deformations within a matrix composed of smaller particles. Small particles are indeed orders of magnitude more abundant than large ones, as shown in Fig. 4. In order to test this hypothesis, we have computed the average non-affine displacements accumulated as a function of the applied strain (analogous to Fig. 10) for subsets of particles. The subsets are generated considering only the particles whose size σ_i satisfies the condition $\sigma_i \geq \sigma_m + b(\sigma_M - \sigma_m)$, where σ_m and σ_M are the smallest and the largest size possible for the specified polydispersity δ (see Table 1). In Fig. 12 we consider two samples, one with low and the other with high polydispersities. We show the non-affine displacement accumulated by the largest particle only, as well as the one averaged over three subsets of particles corresponding to $b = 0$ (all the particles, as in Fig. 10), $b = 0.25$, and $b = 0.75$. Similar to Fig. 11, one can appreciate that the

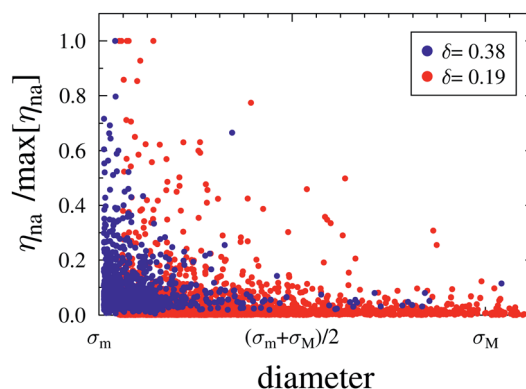


Fig. 11 Non-affine displacement as a function of particle diameter, during an irreversible event.

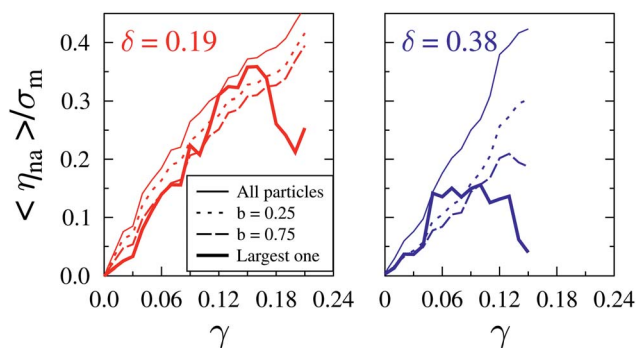


Fig. 12 Average non-affine displacements for particles with size $\sigma_i \geq \sigma_m + b(\sigma_M - \sigma_m)$. σ_m and σ_M are the smallest and the largest size possible for the specified polydispersity δ (see Table 1).

largest particles are characterized by relatively smaller non-affine displacements. In addition to that, for low cumulative strains all particles appear to contribute similar to the non-affine displacements, while for relatively higher γ the contribution of the largest particles drops significantly. This effect becomes more dramatic upon increasing the polydispersity. In particular, for the higher polydispersity considered here, the regime in which the strain is localized in regions densely populated by small particles seems to coincide with the onset of the non-linear response ($\gamma \approx 0.05$). This supports our interpretation that large particles behave as inclusions after the onset of yielding, and that they need to be excluded from the subsequent plastic flow. The emerging physical picture is that high polydispersity, which allows to achieve higher packing fractions, may hinder the non-affine rearrangements of small particles that go around and exclude large ones. This can result in broadening of the elastic regime in Fig. 8 (e.g., until $\gamma \approx 0.05$ instead of $\gamma \approx 0.02$ detected for the systems with low and no polydispersity), until the largest particles are *unlocked* and the system yields (Fig. 12).

4 Conclusions

In this work we have developed new understanding of the mechanical response of dense, out-of-equilibrium assemblies of interacting, polydisperse, colloidal particles, with the aim of linking the observed behaviors to the mechanics of the C–S–H gels in cement pastes. Our colloidal approach allows us to investigate the range of length-scales between nanometers and micrometers that is still largely not understood in this class of materials, although it is crucial for the development of structural complexity and nontrivial mechanical response. The potentials of effective interaction that we developed are able to include a few features obtained from experiments and molecular scale simulations of calcium–silicate–hydrates (e.g., the polydispersity and the strain at rupture). We have showed here that accounting for the interfacial zone at the “contact” points between the nanoparticles is key to obtain elastic constants of the model gels that agree well with the results from nanoindentation experiments. This led to a significant improvement of the computed elastic constants, compared to a previous version of our model.¹⁵

We use a Monte Carlo space-filling algorithm to generate the model colloidal structures, followed by relaxation to zero stress. The algorithm is based on random insertion of polydisperse particles into a simulation box, and on minimization of the total interaction energy. This protocol has the advantage of producing systems with high packing fractions, in the range of those measured experimentally by nanoindentation on the C–S–H gel. We find that the resulting distributions of particle sizes (and hence structural heterogeneities) inside the simulation box are of geometric type, a characteristic that is consistent with the results of small angle neutron scattering experiments.^{17,42}

The response of our model structures to shear deformation is elastic at small applied strain, but some marked nonlinearities appear at greater strain levels and eventually the systems undergo yielding. After yielding, the shear stress oscillates

around a maximum constant value that is a measure of the shear strength of our model C–S–H gels. We have found that the shear strength increases very significantly with the polydispersity. This is consistent with the fact the higher polydispersity allows for denser packing. We have also found that the range of strain in which the response of the system is elastic, *i.e.* reversible upon unloading, increases with the polydispersity. This implies that the strength of our model gels increases faster than the elastic constants, upon increasing the polydispersity, *viz.* the packing density. A similar trend is also shown by nanoindentation measurements on real C–S–H gel.¹⁰

Structural heterogeneities are certainly important for the mechanics of these complex, soft matter systems, for example with regard to strain localization and triggering of non-linear responses. Despite critical for the performance of the material, these issues remain mainly unexplored. We have investigated the accumulation of irreversible processes in the mechanical response, by relaxing our configurations from different levels of applied strain, back to zero shear stress. The results show that once yielding is triggered, the accumulation of irreversible strain is similar for all the model systems irrespective of their polydispersity. Nevertheless, the amount of irreversibility quantified by the decrease of total interaction energy during the shear tests is remarkably smaller in the highly polydisperse systems. We have shown that the mechanisms of accumulation of irreversible deformations (“plastic rearrangements”) are discrete events, whose signature is an abrupt drop of shear stresses and pressure, accompanied by large non-affine displacements of the particles. By monitoring the non-affine displacements of subsets of particles within certain ranges of sizes, we have shown that small particles undergo larger non-affine displacement during a plastic event, *i.e.* they play a primary role in the accumulation of irreversible deformations. By contrast, large particles behave as inclusions that hardly move and that need to be “excluded” by the motion of the rest of the system in order for yielding to occur. This may be the reason why highly polydisperse systems display a broad initial elastic regime: it is hard to circumvent large particles and exclude them from the plastic flow.

In conclusion, our colloidal description of C–S–H gels has allowed gaining significant new insight into the role of nano-scale structural heterogeneities and in particular polydispersity. This opens new, unexplored ways to optimize the mechanical performance of the C–S–H gels, provided we also improve our knowledge on how the complex chemistry of the cement pastes affects the formation process of these gels, the size of the colloidal units, and the interactions between them. A deeper understanding of the issues addressed here and suggested by our soft-matter physics approach can be the key to the development of innovative and more sustainable cements.

References

- 1 G. W. Scherer, *Cem. Concr. Res.*, 1999, **29**, 1149–1157.
- 2 H. M. Jennings, *Cem. Concr. Res.*, 2000, **30**, 101–116.
- 3 A. Nonat, *Cem. Concr. Res.*, 2004, **34**, 1521–1528.

- 4 L. Nicoleau, T. Gädt, L. Chitu, G. Maier and O. Paris, *Soft Matter*, 2013, **9**, 4864–4874.
- 5 H. M. Jennings, *J. Am. Ceram. Soc.*, 1986, **69**, 614–618.
- 6 S. Garraut, E. Finot, E. Lesniewska and A. Nonat, *Mater. Struct.*, 2005, **38**, 435–442.
- 7 S. Garraut, T. Behr and A. Nonat, *J. Phys. Chem. B*, 2006, **110**, 270–275.
- 8 G. Constantinides and F.-J. Ulm, *J. Mech. Phys. Solids*, 2007, **55**, 64–90.
- 9 M. Vandamme and F.-J. Ulm, *Proc. Natl. Acad. Sci. U. S. A.*, 2009, **106**, 10552–10557.
- 10 M. Vandamme, F.-J. Ulm and P. Fonollosa, *Cem. Concr. Res.*, 2010, **40**, 14–26.
- 11 R. J.-M. Pellenq, A. Kushima, R. Shahsavari, K. J. Van Vliet, M. J. Buehler, S. Yip and F.-J. Ulm, *Proc. Natl. Acad. Sci. U. S. A.*, 2009, **106**, 16102–16107.
- 12 H. Manzano, S. Moeini, F. Marinelli, A. C. Van Duin, F.-J. Ulm and R. J.-M. Pellenq, *J. Am. Chem. Soc.*, 2012, **134**, 2208–2215.
- 13 S. Bishnoi and K. L. Scrivener, *Cem. Concr. Res.*, 2009, **39**, 266–274.
- 14 J. W. Bullard, E. Enjolras, W. L. George, S. G. Satterfield and J. E. Terrill, *Modell. Simul. Mater. Sci. Eng.*, 2010, **18**, 025007.
- 15 E. Masoero, E. Del Gado, R.-M. Pellenq, F.-J. Ulm and S. Yip, *Phys. Rev. Lett.*, 2012, **109**, 155503.
- 16 W.-S. Chiang, E. Fratini, P. Baglioni, D. Liu and S.-H. Chen, *J. Phys. Chem. C*, 2012, **116**, 5055–5061.
- 17 S. Brisard and P. Levitz, *Phys. Rev. E: Stat., Nonlinear, Soft Matter Phys.*, 2013, **87**, 013305.
- 18 H. Taylor, *Adv. Cem. Based Mater.*, 1993, **1**, 38–46.
- 19 X. Cong and R. J. Kirkpatrick, *Adv. Cem. Based Mater.*, 1996, **3**, 144–156.
- 20 I. Richardson, *Cem. Concr. Res.*, 1999, **29**, 1131–1147.
- 21 R. J.-M. Pellenq and H. Van Damme, *MRS Bull.*, 2004, **29**, 319–323.
- 22 B. Jönsson, A. Nonat, C. Labbez, B. Cabane and H. Wennerström, *Langmuir*, 2005, **21**, 9211–9221.
- 23 H. Hertz, *Miscellaneous Papers*, MacMillan & Co., 1896, pp. 163–183.
- 24 H. Manzano, E. Masoero, I. Lopez Arbeloa and H. M. Jennings, *Soft Matter*, 2013, **9**, 7333–7341.
- 25 H. Brouwers, *Phys. Rev. E: Stat., Nonlinear, Soft Matter Phys.*, 2006, **74**, 031309.
- 26 M. Hermes and M. Dijkstra, *Europhys. Lett.*, 2010, **89**, 38005.
- 27 D. Frankel and B. Smit, *Understanding molecular simulation: From algorithms to applications*, San Diego, Academic, 1996.
- 28 R. Najafabadi and S. Yip, *Scr. Metall.*, 1983, **17**, 1199–1204.
- 29 T. Hill, *Statistical Mechanics*, McGraw-Hill, New York, 1956.
- 30 J. Lutsko, *J. Appl. Phys.*, 1989, **65**, 2991–2997.
- 31 J. F. Nye, *Physical properties of crystals: their representation by tensors and matrices*, Oxford University Press, 1985.
- 32 R. M. Nedderman, *Statics and kinematics of granular materials*, Cambridge University Press, 2005.
- 33 T. S. Majmudar and R. P. Behringer, *Nature*, 2005, **435**, 1079–1082.
- 34 A. V. Mokshin and J.-L. Barrat, *Phys. Rev. E: Stat., Nonlinear, Soft Matter Phys.*, 2008, **77**, 021505.
- 35 R. Blaak, S. Auer, D. Frenkel and H. Löwen, *Phys. Rev. Lett.*, 2004, **93**, 068303.
- 36 S. Butler and P. Harrowell, *Phys. Rev. E: Stat. Phys., Plasmas, Fluids, Relat. Interdiscip. Top.*, 1995, **52**, 6424.
- 37 J. J. Cerdà, T. Sintes, C. Holm, C. Sorensen and A. Chakrabarti, *Phys. Rev. E: Stat., Nonlinear, Soft Matter Phys.*, 2008, **78**, 031403.
- 38 S. Alexander, *Phys. Rep.*, 1998, **296**, 65–236.
- 39 C. E. Maloney and A. Lemaitre, *Phys. Rev. E: Stat., Nonlinear, Soft Matter Phys.*, 2006, **74**, 016118.
- 40 A. Tanguy, J. Wittmer, F. Leonforte and J.-L. Barrat, *Phys. Rev. B: Condens. Matter Mater. Phys.*, 2002, **66**, 174205.
- 41 S. P. Timoshenko and J. M. Gere, *Theory of elastic stability*, Courier Dover Publications, 2012.
- 42 A. J. Allen, J. J. Thomas and H. M. Jennings, *Nat. Mater.*, 2007, **6**, 311–316.